

## Molybdenum isotopes in plume-influenced MORBs reveal recycling of ancient anoxic sediments

Q. Ahmad, M. Wille, C. Rosca, J. Labidi, T. Schmid, K. Mezger, S. König

### Supplementary Information

The Supplementary Information includes:

- Section S-1: Geochemical Background of the Samples
- Section S-2: Potential Controls on the Mo Isotope Variability of S-MAR Basalts
- Section S-3: Origin of Enriched Mantle
- Section S-4: Analytical Methods
- Section S-5: Misfit Model
- Supplementary Information References

### Section S-1: Geochemical Background of the Samples

The studied samples are fresh basaltic glasses that were dredged from the South-Mid Atlantic Ridge (S-MAR) during the RV *Maurice Ewing* cruise EW93-09 (Douglass *et al.*, 1995, 1999). All samples were well-characterised in terms of radiogenic isotopes (Sr, Nd, Hf, and Pb) (Douglass *et al.*, 1999; Andres *et al.*, 2002), S isotopes (Labidi *et al.*, 2013), Se isotopes (Yierpan *et al.*, 2020), noble gases (Moreira *et al.*, 1995; Sarda *et al.*, 2000), and major and trace element abundances (le Roux *et al.*, 2002a, 2002b, 2002c; Kelley *et al.*, 2013). This makes the selected sample suite ideal for investigating their Mo isotope signature.

The most prominent feature in the S-MAR is the localised interaction between the ambient asthenospheric mantle and the Discovery and Shona mantle plumes (Fig. S-1). A variety of recycled components have been suggested to be incorporated in these mantle plumes based on radiogenic and stable isotope systematics (Fig. S-2; see references above).

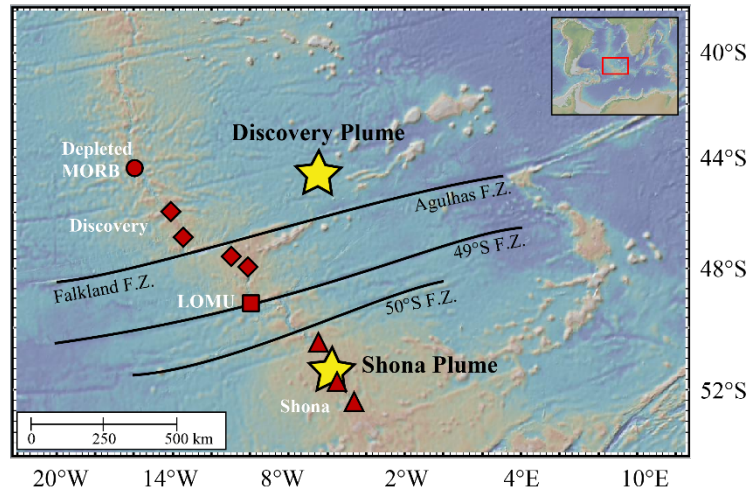


**Figure S-1** Sample locations along the S-MAR together with the Discovery and Shona plume, as well as tectonic fracture zones (F.Z.). Figure made with GeoMapApp ([www.geomapapp.org](http://www.geomapapp.org)).

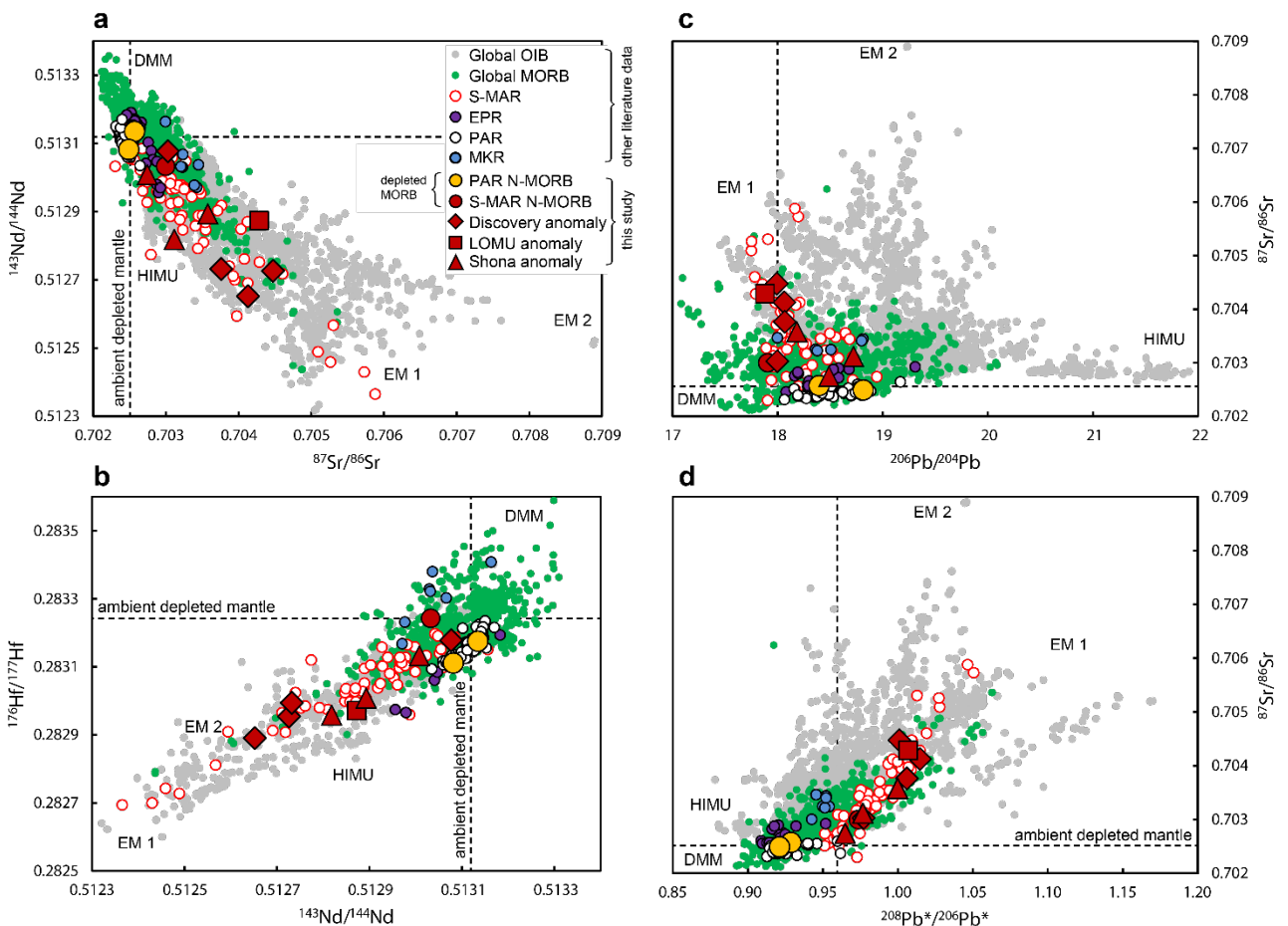


**Figure S-2** Radiogenic isotope data for the studied S-MAR and PAR glasses, modified after Yierpan *et al.* (2020). Shown for comparison are a global compilation of MORB and OIB (Stracke, 2012 and references therein). MORBs (and seamounts) near the East Pacific Rise (EPR) (Chen *et al.*, 2022 and references therein), Mohns-Knipovich ridges (MKR) (Bezard *et al.*, 2016), and PAR (Hamelin *et al.*, 2011 and references therein) are plotted for comparison. A more detailed precompilation of S-MAR basalts can be found in Labidi *et al.* (2013). Dashed lines indicate the composition of the S-MAR ambient depleted mantle (Douglass *et al.*, 1999; Andres *et al.*, 2002). In (d),  $^{208}\text{Pb}^*/^{206}\text{Pb}^*$  exemplifies the time-integrated Th/U ratios (Stracke, 2012).

Two additional samples from the Pacific-Antarctic Ridge (PAR) complement existing PAR-MORB Mo isotope data (Bezard *et al.*, 2016). This setting is dominantly sourced by depleted mantle being devoid of any deep mantle plume influence (*e.g.*, Hamelin *et al.*, 2011) with radiogenic Sr and Nd isotope signature similar to the ambient depleted mantle (ADM) constrained for the S-MAR suite (Table S-2; Douglass *et al.*, 1999; Andres *et al.*, 2002).

## Section S-2: Potential Controls on the Mo Isotope Variability of S-MAR Basalts

Observed correlations between  $\delta^{98/95}\text{Mo}$  and  $^{143}\text{Nd}/^{144}\text{Nd}$  or  $^{176}\text{Hf}/^{177}\text{Hf}$  (Figs. 1, S-4a) exclude post-emplacment seawater alteration effects on the Mo isotope composition, as seawater incorporation is insensitive to relatively fluid-immobile Nd or Hf (see Labidi *et al.*, 2013). This is also supported by Cl/K ratios close to the range of global MORB (Table S-1) (Labidi *et al.*, 2013). Also unlikely is isotope fractionation due to segregation of an isotopically heavy sulfide melt at low melting degrees, which results into an isotopically light silicate melt (Liang *et al.*, 2017). The studied samples were sulfide-saturated during melting (Labidi *et al.*, 2013 and references therein), however, there is no correlation between  $\delta^{98/95}\text{Mo}$  and Mo/Ce, with Ce being similarly incompatible during mantle melting but Mo being more compatible in presence of a segregated sulfide melt. Furthermore, a potential sulfide melt segregation would have removed any relationship between  $\delta^{98/95}\text{Mo}$ , and radiogenic isotopes (see Labidi *et al.*, 2013). This covariation together with lack of covariations between  $\delta^{98/95}\text{Mo}$  and MgO or Mg#, and overall high MgO contents (Table S-1) suggests that also fractional crystallisation during differentiation is not the cause of the observed Mo isotope variation (*e.g.*, Voegelin *et al.*, 2014). This is in line with other tholeiitic systems (*e.g.*, Yang *et al.*, 2015; Bezard *et al.*, 2016).

Elemental systematics of S-MAR basalts suggest mixing of ambient mantle with low-degree melts ( $F = 2\text{--}3\%$ ; le Roux *et al.*, 2002b). Previously, elevated  $\delta^{98/95}\text{Mo}$  in lavas from the EPR (devoid of a mantle plume component) were interpreted to reflect mixing of depleted MORB with an isotopically heavy end member of magmatic origin without contribution of recycled crustal components (Chen *et al.*, 2022). The authors argued that this heavy end member is an ancient ( $>1\text{ Ga}$ ) low-degree melt ( $F = 0.2\%$ ) of depleted mantle material that led to an initial fractionation of  $\delta^{98/95}\text{Mo}$  (due to different magmatic compatibilities of  $\text{Mo}^{4+}$  and  $\text{Mo}^{6+}$ ; McCoy-West *et al.*, 2019), similar incompatible elements (*e.g.*, Nb/Zr), and further parent-daughter ratios of radiogenic isotopes. This explains the observed correlation of  $\delta^{98/95}\text{Mo}$  and radiogenic isotopes of Pb, Nd, and Sr (Chen *et al.*, 2022). In the S-MAR sample suite, the trace element ratios are accompanied by radiogenic isotope systematics attributable to an enriched mantle 1 (EM1) signature requiring a higher initial Rb/Sr, lower Sm/Nd and Lu/Hf, and similar U/Pb compared to DMM (Fig. S-2). These signatures, however, are primary and cannot be explained by low- $F$  melting of plume mantle material (le Roux *et al.*, 2002b). Furthermore, plume-material is pre-enriched in isotopically heavy S and Se prior to low- $F$

melting (Labidi *et al.*, 2013; Yierpan *et al.*, 2020). The question remains, if heavy Mo is primary or if it is generated during low- $F$  mantle melting. If we consider a low- $F$  melting of  $F = 2.5\%$  melting (le Roux *et al.*, 2002b) of plume material ( $T = 1200\text{ °C}$ ;  $\text{Mo}^{6+}/\Sigma\text{Mo} = 0.99$ ), we would expect a maximum isotope shift of  $\Delta^{98/95}\text{Mo}_{\text{max}}$  of  $\sim 0.085\text{ ‰}$  between pyroxenite melt and DMM ( $F = 15\%$ ) (McCoy-West *et al.*, 2019). A mixture of both of these end members with 20 % pyroxenite contribution in our heaviest sample EW9309 33D-1g (le Roux *et al.*, 2002b) would lead to a maximum  $\Delta^{98/95}\text{Mo}_{\text{max}}$  of 0.059 ‰ (melting model from Wang and Becker, 2018). This value is likely lower ( $\Delta^{98/95}\text{Mo}_{\text{max}} = 0.040\text{ ‰}$ ) when considering lower N-MORB like [Mo] of pyroxenite melts, as there is no covariation of  $\delta^{98/95}\text{Mo}$  and Mo/Ce (Fig. S-5). Moreover, these pyroxenites are formed along the plume-adiabat, which is hotter than the N-MORB adiabat, lowering further the isotopic fractionation induced by low- $F$  melting. Furthermore, we do not observe a correlation of  $\delta^{98/95}\text{Mo}$  with Pb isotopes, which is inconsistent with the increase of U/Pb during ancient low- $F$  melting (Chen *et al.*, 2022). In contrast, we observe LOMU-samples that carry an isotopic heavy signature, which is consistent with an *e.g.*, Proterozoic sediment contribution (*e.g.*, Rehkämper and Hofmann, 1997; Douglass *et al.*, 1999; Andres *et al.*, 2002). As correlations between radiogenic isotopes and  $\delta^{34/32}\text{S}$ ,  $\delta^{82/76}\text{Se}$ , and  $\delta^{98/95}\text{Mo}$  (*e.g.*, Fig. 1, S-4b) cannot be explained by magmatic processes or post-emplacement alteration (see Labidi *et al.*, 2013; Yierpan *et al.*, 2019, 2020, 2021), this relationship is in strong support of recycling of enriched mantle components with  $\delta^{98/95}\text{Mo} >$  depleted mantle.



**Table S-1** Average and individual Mo isotope and elemental data of analysed MORBs from S-MAR and PAR. MgO and calculated Cl/K are from (le Roux *et al.*, 2002a; Labidi *et al.*, 2013). Individual measurements represent separate sample digestions and chromatographic separations. \*Internal precision on a sample run (over 80 cycles) is reported as 2 standard error (2 s.e.).

Sample	Type	Individual measurements			Mean values				
		$\delta^{98/95}\text{Mo}$ (‰)	2 s.e.* (‰)	Mo ( $\mu\text{g/g}$ )	$\delta^{98/95}\text{Mo}$ (‰)	2 s.d. (‰)	Mo ( $\mu\text{g/g}$ )	MgO (wt. %)	Cl/K
EW9309 40D-1g	Depleted N-MORB	-0.226	0.015	0.254	-0.231	0.064	0.254	8.30	0.11
		-0.201	0.022	0.255					
		-0.265	0.020	0.254					
EW9309 33D-1g	Discovery influenced MORB (North)	-0.100	0.013	1.25	-0.098	0.048	1.25	7.83	0.04
		-0.073	0.020	1.25					
		-0.121	0.013	1.25					
EW9309 28D-1g	Discovery influenced MORB (North)	-0.191	0.018	0.168	-0.239	0.136	0.169	8.22	0.06
		-0.287	0.018	0.170					
EW9309 2D-1g	Discovery influenced MORB (South)	-0.122	0.020	0.665	-0.148	0.074	0.663	6.24	0.03
		-0.174	0.014	0.661					
EW9309 4D-3g	Discovery influenced MORB (South)	-0.136	0.015	0.539	-0.152	0.077	0.528	7.60	0.04
		-0.124	0.020	0.527					
		-0.195	0.016	0.517					
EW9309 9D-3g	LOMU MORB	-0.167	0.017	0.654	-0.183	0.045	0.654	8.67	0.06
		-0.199	0.015	0.654					
EW9309 15D-1g	Shona influenced MORB	-0.199	0.028	0.363	-0.207	0.023	0.364	7.81	0.08
		-0.215	0.019	0.364					
EW9309 21D-1g	Shona influenced MORB	-0.179	0.027	0.587	-0.188	0.024	0.586	7.10	0.05
		-0.196	0.013	0.585					
EW9309 22D-3g	Shona influenced MORB	-0.155	0.019	1.03	-0.187	0.090	1.03	4.83	0.07
		-0.219	0.017	1.03					



Table S-1 continued.

Sample	Type	Individual measurements			Mean values				
		$\delta^{98/95}\text{Mo}$ (‰)	2 s.e.* (‰)	Mo ( $\mu\text{g/g}$ )	$\delta^{98/95}\text{Mo}$ (‰)	2 s.d. (‰)	Mo ( $\mu\text{g/g}$ )	MgO (wt. %)	Cl/K
PAC2 DR33-1	<i>Pacific-Antarctic ridge</i> Depleted N-MORB	-0.225	0.018	0.470	-0.245	0.062	0.462	6.63	-
		-0.228	0.028	0.461					
		-0.281	0.016	0.454					
PAC1 CV-02g	Depleted N-MORB	-0.249	0.016	0.213	-0.297	0.116	0.215	7.74	-
		-0.280	0.031	0.213					
		-0.361	0.021	0.218					
AGV-2	Andesite	-0.192	0.015	2.13	-0.194	0.042	2.14	-	-
		-0.211	0.019	2.11					
		-0.179	0.012	2.19					
BHVO-2	Basalt	-0.092	0.015	3.43	-0.108	0.032	3.68	-	-
		-0.099	0.017	4.64					
		-0.132	0.015	2.96					
W-2a	Diabase	-0.100	0.018	0.462	-0.087	0.053	0.452	-	-
		-0.104	0.021	0.455					
		-0.057	0.010	0.439					



### Section S-3: Origin of Enriched Mantle

Different recycled components (*e.g.*, sub-continental mantle, lower continental crust, oceanic crust, and sediment) in the mantle source of the S-MAR (Douglass *et al.*, 1999; Andres *et al.*, 2002; le Roux *et al.*, 2002c; Labidi *et al.*, 2013; Yierpan *et al.*, 2020) can have an influence on  $\delta^{98/95}\text{Mo}$  of the samples. Sub-continental mantle can be excluded as a significant component, since worldwide peridotites have a MORB-like  $\delta^{98/95}\text{Mo}$  ( $-0.206 \pm 0.05$  ‰; Liang *et al.*, 2017). An aqueous fluid expelled from subducted crust can influence the mantle composition leading to elevated  $\delta^{98/95}\text{Mo}$  and [Mo] (*e.g.*, Ahmad *et al.*, 2021); however, we observe correlations between  $\delta^{98/95}\text{Mo}$  and aqueous fluid-immobile Nd and Hf isotopes (Figs. 1, S-4a) and no covariation is observed with fluid proxies, such as Ba/Th ( $R^2 = 0.1$ ). There is no direct estimate of  $\delta^{98/95}\text{Mo}$  of the lower continental crust (LCC), however, cumulates which possibly reside in the LCC, likely incorporate preferentially light Mo isotopes (Wille *et al.*, 2018; Nebel-Jacobsen *et al.*, 2021) and are unsuitable candidates to explain Mo signatures in the basalt samples. Apart from a clear EM1 affinity, two samples analysed here show a trend towards HIMU (Fig. S-2), thus a signature of recycled AOC. However,  $^{206}\text{Pb}/^{204}\text{Pb}$  ratios do not correlate with  $\delta^{98/95}\text{Mo}$  and most radiogenic  $^{206}\text{Pb}/^{204}\text{Pb}$  values are accompanied with depleted mantle-like  $\delta^{98/95}\text{Mo}$  (Fig. S-4c). This leads to the conclusion that a significant influence of recycled AOC is unlikely. Furthermore, prograde subduction metamorphism can modify the AOC Mo isotopic signature to lighter values than mantle due to AOC and serpentinite dehydration (Freymuth *et al.*, 2015; Chen *et al.*, 2019), which is also not observed. Oxidised Phanerozoic subducted metasediments are characterised by  $\delta^{98/95}\text{Mo}$  lower than mantle (Ahmad *et al.*, 2021) and b) modelled Mid-Proterozoic sediment recycling ages (Douglass *et al.*, 1999; Andres *et al.*, 2002; Labidi *et al.*, 2013) suggest anoxic deep ocean redox conditions during the Proterozoic (*e.g.*, Lyons *et al.*, 2014). Based on previous stable S and Se studies, the recycled sediment component is likely anoxic and experienced negligible subduction-related S and Se mobilisation (Labidi *et al.*, 2013; Yierpan *et al.*, 2020) indicating a stable sedimentary sulfide phase (and potential Mo host) during potential hotter subduction zone conditions in the Proterozoic. This is in line with a previous Mo isotope study on a partially melted Archean eclogite, which indicates stable Mo host phases such as rutile and sulfide (Greaney *et al.*, 2018). Preservation of isotopically heavy Se and Mo in the recycled component further indicates that there was negligible modification by oxidising fluids during anoxic Proterozoic sediment subduction (see König *et al.*, 2021; see discussion in the main text). In line with previous investigations showing covariations between  $f\text{O}_2$ -sensitive stable Se-S isotope systematics and radiogenic isotopes,  $\delta^{98/95}\text{Mo}$  higher than depleted mantle, and overall low Mo mobility during anoxic sediment subduction (see discussion in the main text) we suggest that an anoxic Proterozoic sediment contribution to the S-MAR mantle source is the most likely scenario for the observed heavy Mo isotope enrichment in our samples.



## Section S-4: Analytical Methods

Molybdenum purification and isotope analysis was conducted in the clean laboratory facilities at the Institute of Geological Sciences, University of Bern. For all samples, enough powder was weighed to have 25–50 ng Mo for analysis. The material was spiked with an enriched isotope tracer solution ( $^{97}\text{Mo}$ - $^{100}\text{Mo}$  double spike). The samples were then dissolved in concentrated single distilled acids in the following sequence: (i) concentrated HF-HNO<sub>3</sub> (3:1 mixture), (ii) concentrated HNO<sub>3</sub>, (iii) 6 M HCl in Savillex™ Teflon vials. The dissolved samples were processed through anion- and cation exchange columns to obtain a clean Mo separate (Wille *et al.*, 2013). In the first step, samples were taken up in 4 M HCl and passed through Dowex 1X8, 200–400 mesh, anion resin. In a second step, the sample material was taken up in 0.5 M HCl and passed through Dowex 50WX8 200–400 mesh, cation exchange resin. Stable Mo isotope measurements were carried out on a Neptune Plus MC-ICPMS coupled with an Aridus II desolvating nebuliser with an uptake rate of 100–150  $\mu\text{L min}^{-1}$  (details are provided in Ahmad *et al.*, 2021). Six Mo isotopes ( $^{94}\text{Mo}$ ,  $^{95}\text{Mo}$ ,  $^{96}\text{Mo}$ ,  $^{97}\text{Mo}$ ,  $^{98}\text{Mo}$  and  $^{100}\text{Mo}$ ) were measured as well as  $^{99}\text{Ru}$  and  $^{101}\text{Ru}$  to monitor potential isobaric interference. We used resistors with  $10^{-11} \Omega$  to analyse all isotopes except  $^{101}\text{Ru}$ , which was measured using a  $10^{-12} \Omega$  resistor. For analyses, we have used a combination of ‘H’ Ni sampler cone and ‘X’ Ni skimmer cone and obtained  $\sim 120$  V/ppm on  $^{95}\text{Mo}$ . We used a double spike correction method based on an iterative calculation procedure (see Siebert *et al.*, 2001). The total procedural blank was between 0.22 to 0.65 ng. We present all data in the  $\delta$  notation and relative to NIST SRM 3134 in ‰ (Greber *et al.*, 2012; Goldberg *et al.*, 2013) with an interference correction based on  $^{99}\text{Ru}$ :

$$\delta^{98/95}\text{Mo} = \left( \frac{\left( \frac{^{98}\text{Mo}}{^{95}\text{Mo}} \right)_{\text{Sample}}}{\left( \frac{^{98}\text{Mo}}{^{95}\text{Mo}} \right)_{\text{NIST SRM 3134}}} - 1 \right) * 1,000 \quad (\text{S-1})$$

Interference-corrected  $\delta^{98/95}\text{Mo}$  ratios based on  $^{99}\text{Ru}$  and  $^{101}\text{Ru}$  correction were compared to ensure accurate determination of the Ru interference. Background correction was obtained by bracketing samples with measurements of 0.5 M HNO<sub>3</sub> carrier solution on-peak. Sample and background analysis consisted of 80 and 30 cycles, respectively, with a signal integration time of 4.194 s for each cycle. Repeated measurements of the standard NIST SRM 3134 and an in-house J&M standard solution lot 602332B gave an isotopic difference of  $\Delta^{98/95}\text{Mo} = 0.269 \pm 0.017$  ‰ (2 s.d.,  $n = 14$ ), in agreement with Greber *et al.* (2012) and Ahmad *et al.* (2021). Solution standards were measured at a concentration of 25 ppb. Individually digested and chemically purified whole-rock reference materials AGV-2, BHVO-2 and W-2a yielded a  $\delta^{98/95}\text{Mo}$  of  $-0.19 \pm 0.03$  ‰ (2 s.d.,  $n = 3$ ),  $-0.11 \pm 0.04$  ‰ (2 s.d.,  $n = 3$ ) and  $-0.09 \pm 0.05$  ‰ (2 s.d.,  $n = 3$ ), respectively (Table S-1). The



values are within uncertainty of those determined previously (*e.g.*, Burkhardt *et al.*, 2014; Willbold *et al.*, 2016; Zhao *et al.*, 2016). Individual measurements of whole rock reference materials (Table S-1) are within the long-term 2 s.d. external reproducibility of  $\pm 0.05$  ‰ as determined by previous measurements of BHVO-2 (Ahmad *et al.*, 2021). Including these previous BHVO-2 measurements ( $-0.09 \pm 0.05$  ‰,  $n = 10$ ), we consider  $\pm 0.05$  ‰ as the long-term 2 s.d. external reproducibility of our sample measurements. All samples were measured multiple times (after individual digestions and chemical separation) and obtained  $\delta^{98/95}\text{Mo}$  and Mo concentration values were averaged for data presentation and interpretation (Table S-1). All individual sample measurements are within  $\pm 0.05$  ‰ compared to their average  $\delta^{98/95}\text{Mo}$ , except PAR sample PAC CV-02g.

### Section S-5: Misfit Model

The “linear” Mo-Sr(-Nd) isotope sample array (Fig. 1) represents only a small segment relative to the sediment end member (Table S-2), suggesting that a hyperbolic mixing curve could also account for the observed correlation. Mixing of two components (sediment, ‘SED’, and ambient depleted mantle end members, ‘DM’) with different Mo-Sr(-Nd) isotope compositions and concentrations will result in a hyperbola (*cf.* Vollmer, 1976) of the form:

$$Ax + Bxy + Cy + D = 0 \quad (\text{S-2})$$

where

$$A = a_{\text{DM}}b_{\text{SED}}y_{\text{DM}} - a_{\text{SED}}b_{\text{DM}}y_{\text{SED}} \quad (\text{S-3})$$

$$B = a_{\text{SED}}b_{\text{DM}} - a_{\text{DM}}b_{\text{SED}} \quad (\text{S-4})$$

$$C = a_{\text{DM}}b_{\text{SED}}x_{\text{SED}} - a_{\text{SED}}b_{\text{DM}}x_{\text{DM}} \quad (\text{S-5})$$

$$D = a_{\text{SED}}b_{\text{DM}}x_{\text{DM}}y_{\text{SED}} - a_{\text{DM}}b_{\text{SED}}x_{\text{SED}}y_{\text{DM}} \quad (\text{S-6})$$

and

$$x = {}^{87}\text{Sr}/{}^{86}\text{Sr} \text{ or } {}^{143}\text{Nd}/{}^{144}\text{Nd}$$

$$y = \delta^{98/95}\text{Mo}$$

$$\left. \begin{array}{l} a_{\text{SED}} = \text{conc. of Mo} \\ b_{\text{SED}} = \text{conc. of } {}^{86}\text{Sr} (\sim\text{Sr}) \text{ or } {}^{144}\text{Nd} (\sim\text{Nd}) \end{array} \right\} \text{ of the sediment end member with the isotopic composition } (x_{\text{SED}}/y_{\text{SED}})$$

$$\left. \begin{array}{l} a_{\text{DM}} = \text{conc. of Mo} \\ b_{\text{DM}} = \text{conc. of } {}^{86}\text{Sr} (\sim\text{Sr}) \text{ or } {}^{144}\text{Nd} (\sim\text{Nd}) \end{array} \right\} \text{ of the depleted mantle end member with the isotopic composition } (x_{\text{DM}}/y_{\text{DM}}).$$

By inserting Mo, Sr, and Nd concentrations and isotope compositions from the literature (Table S-2) into above equations, this leads to two unknowns of the sediment end member,  $a_{\text{SED}}$  and  $y_{\text{SED}}$ . By varying  $a_{\text{SED}}$

from  $a_{\text{SED}, \text{min}}$  to  $a_{\text{SED}, \text{max}}$  and  $y_{\text{SED}}$  from  $y_{\text{SED}, \text{min}}$  to  $y_{\text{SED}, \text{max}}$ , a total least squares error can be determined for each  $\delta^{98/95}\text{Mo}^{\text{exp}}$  generated at a given  $^{87}\text{Sr}/^{86}\text{Sr}$  or  $^{143}\text{Nd}/^{144}\text{Nd}$  against the observed sample points as:

$$\sum_{i=a_{\text{SED}, \text{min}}}^{a_{\text{SED}, \text{max}}} \sum_{j=y_{\text{SED}, \text{min}}}^{y_{\text{SED}, \text{max}}} \sqrt{\left(\delta^{98/95}\text{Mo}_{i,j}^{\text{exp}} - \delta^{98/95}\text{Mo}^{\text{sample}}\right)^2} \quad (\text{S-7})$$

where  $a_{\text{SED}, \text{min}} = 0.1 \mu\text{g/g}$ ,  $a_{\text{SED}, \text{max}} = 100 \mu\text{g/g}$ ,  $y_{\text{SED}, \text{min}} = -1 \text{‰}$ , and  $y_{\text{SED}, \text{max}} = 1 \text{‰}$ .

In the obtained misfit plot (Fig. 2), the best agreement between potential sediment end member and measured samples is given by the least squares error (blue banana) of the misfit function. The white dashed line indicates the sample amount multiplied by the external 2 s.d. reproducibility to obtain a conservative upper limit of model compositions. The white solid line indicates the contour line of the least squares error obtained (see minimum  $\Delta^{98/95}\text{Mo}$  in Fig. 2a, b) added by  $\Delta^{98/95}\text{Mo} \approx 0.1 \text{‰}$ . For comparison, the compositions of OM-rich sediments sorted by age intervals (Ye *et al.*, 2021; Table S-2), UCC (Greber *et al.*, 2014; Rudnick and Gao, 2014; Voegelin *et al.*, 2014; Freymuth *et al.*, 2015; Willbold and Elliott, 2017; Yang *et al.*, 2017; Greaney *et al.*, 2020;), MORB (Gale *et al.*, 2013; Bezard *et al.*, 2016; Chen *et al.*, 2022;), pelagic Mn-rich and clastic metasediments (Ahmad *et al.*, 2021), and blueschists and MORB-type eclogites (Chen *et al.*, 2019; Ahmad *et al.*, 2021) are plotted (Fig. 2).

Additional scenarios considered for misfit calculations, such as 1 Ga and 2 Ga model sediments, are plotted in Figure S-3 and show least squares errors similar to those in Figure 2. This indicates that a mid-Proterozoic UCC-like sediment with minor authigenic Mo enrichment is a likely sediment end member (see main text).

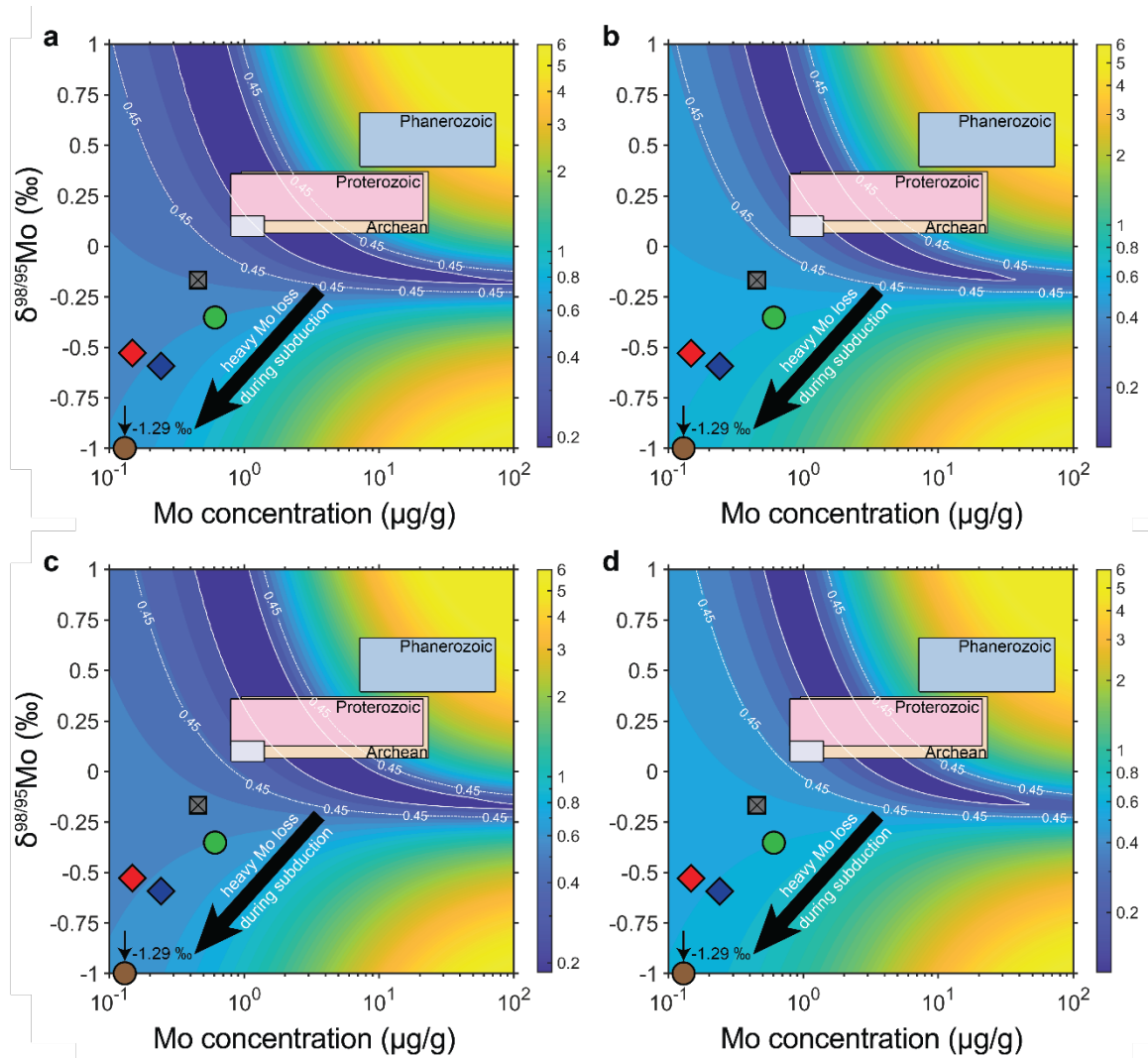


**Figure S-3** Misfit calculation based on mixing parameters reported in Figure 2 and adjusted time-integrated Sr and Nd isotope compositions of the model sediment: **(a)**  $^{87}\text{Sr}/^{86}\text{Sr}$  (1 Ga) = 0.7173; **(b)**  $^{143}\text{Nd}/^{144}\text{Nd}$  (1 Ga) = 0.5115; **(c)**  $^{87}\text{Sr}/^{86}\text{Sr}$  (2 Ga) = 0.7233; **(d)**  $^{143}\text{Nd}/^{144}\text{Nd}$  (2 Ga) = 0.5119.

**Table S-2** Parameters from the two-component mixing model (Fig. 2) and compositions of marine sediments.

	$\delta^{98/95}\text{Mo}$ (‰)	[Mo] ( $\mu\text{g/g}$ )	$^{87}\text{Sr}/^{86}\text{Sr}$	Sr ( $\mu\text{g/g}$ )	$^{143}\text{Nd}/^{144}\text{Nd}$	Nd ( $\mu\text{g/g}$ )
<b>End members</b>						
Ambient depleted mantle	$-0.245 \pm 0.05^{\text{A}}$	$0.025 \pm 0.007$	0.70250 or $0.702488 \pm 0.000032$	$9.80 \pm 1.86$	0.51312 or $0.513135 \pm 0.00002$	$0.713 \pm 0.05$
1.5 Ga old recycled pelagic sediment	$0.78 \pm 0.20^{\text{B}}$ or $0.12 \pm 0.06^{\text{B}}$	$0.76^{\text{B}}$ or $2.98^{\text{B}}$	0.7203	$300 \pm 17$	0.5117	$85 \pm 5.2^{\text{C}}$
<b>Marine sediments<sup>D</sup></b>						
Archean	$0.218 \pm 0.150$ ( $M = 19, N = 417$ )	$4.70^{+18.4}_{-3.75}$ ( $M = 19, N = 744$ )				
Proterozoic	$0.244 \pm 0.114$ ( $M = 51, N = 696$ )	$4.10^{+17.0}_{-3.30}$ ( $M = 53, N = 1262$ )				
Phanerozoic	$0.528 \pm 0.132$ ( $M = 48, N = 882$ )	$22.9^{+49.7}_{-15.7}$ ( $M = 48, N = 1154$ )				

The mixing trends are generated using compositions of the Pacific/ambient depleted mantle or the most depleted MORB: PAC2 DR33-1 and PAC1 CV-02g (in italics). Uncertainties on mixing end member elemental concentrations (Rehkämper and Hofmann, 1997; Salters and Stracke, 2004; Labidi *et al.*, 2013; Plank, 2014; Yierpan *et al.*, 2020) and on [Mo]- $\delta^{98/95}\text{Mo}$  values of the marine sediment compilation (Ye *et al.*, 2021) are all  $1\sigma$  (except [Mo] uncertainty in depleted mantle, see Salters and Stracke, 2004).

Pelagic sediment and ambient mantle end member isotope compositions (Rehkämper and Hofmann, 1997; Andres *et al.*, 2002; le Roux *et al.*, 2002c; Labidi *et al.*, 2013; Yierpan *et al.*, 2020) are reported with  $1\sigma$  uncertainties, (except  $\delta^{98/95}\text{Mo}$  uncertainty, which is reported as  $2\sigma$ ).  $M$  = number of age averaged data,  $N$  = number of different sediment samples from the literature.

<sup>A</sup> The Mo isotope composition of the Pacific-Antarctic Ridge (PAR) basalts can be used as the depleted mantle end member, because their Sr and Nd isotope composition match the S-MAR ambient depleted mantle isotopic composition determined previously (Douglass *et al.*, 1999; Andres *et al.*, 2002). The Mo isotope composition of the depleted N-MORB DR33-1g ( $\delta^{98/95}\text{Mo} = -0.245 \pm 0.05$  ‰) matches the light isotope composition of Phanerozoic Gorgona komatiites ( $\delta^{98/95}\text{Mo} = -0.18$  to  $-0.25$  ‰, McCoy-West *et al.*, 2019) and the lighter end of PAR basalts measured previously ( $\delta^{98/95}\text{Mo} = -0.06$  to  $-0.24$  ‰, excluding the three heavy outliers; Bezard *et al.*, 2016). Because  $\delta^{98/95}\text{Mo}$  values of S-MAR basalts (and MORBs from EPR and PAR, Fig. 1) extend towards slightly lower values (but still within error) compared to the mean depleted mantle estimate (e.g., McCoy-West *et al.*, 2019), we use this lower end of observed literature values for the ambient depleted mantle. The depleted N-MORB CV-02g ( $\delta^{98/95}\text{Mo} = -0.297 \pm 0.05$  ‰), however, represents an outlier being lighter than this range (but still within error) and is excluded in this model.



**Table S-2 continued.**

<sup>B</sup> Obtained best fit parameters from linear correlation between Mo-Sr isotope and Mo-Nd isotope (italic font) trend and the Mo, Sr, and Nd contents of depleted mantle and 1.5 Ga pelagic sediment (see above). Note the discrepancy between both  $\delta^{98/95}\text{Mo}$  and [Mo] obtained from both relationships (Fig. 1).

<sup>C</sup> Assigned relative error from GLOSS-II (Plank, 2014) as there was no uncertainty considered for pelagic sediment Nd content.

<sup>D</sup> Marine sediment values of different eons are log-normal means of sediments sorted by age intervals (>1 Myr) from the literature (see compilation of Ye *et al.*, 2021). The literature data represent mostly shallow-marine (continental shelf/closed basins) sediments from anoxic/euxinic settings, where *e.g.*, sulfate reduction leads to higher authigenic accumulation of isotopically heavy Mo from seawater compared to lower Mo accumulation in the anoxic deep sea (see main text).



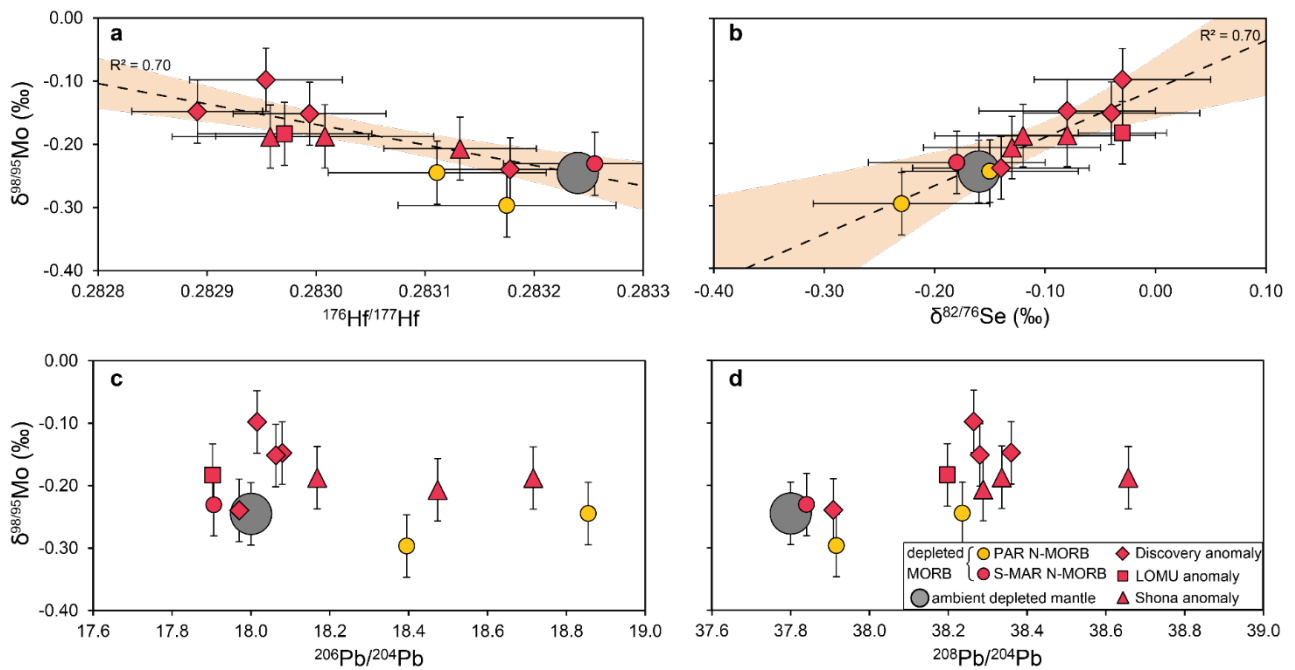


**Figure S-4** Covariation diagram of S-MAR samples with: **(a)**  $\delta^{98/95}\text{Mo}$  vs.  $^{176}\text{Hf}/^{177}\text{Hf}$ ; **(b)**  $\delta^{98/95}\text{Mo}$  vs.  $\delta^{82}\text{Se}$  **(c)**  $\delta^{98/95}\text{Mo}$  vs.  $^{206}\text{Pb}/^{204}\text{Pb}$ ; and **(d)**  $\delta^{98/95}\text{Mo}$  vs.  $^{208}\text{Pb}/^{204}\text{Pb}$ . Error bars indicate 2 s.d. external reproducibility. External reproducibility on each isotope value is considered for regressions in **(a)** and **(b)**, and shaded areas indicate 95 % CI error envelope. PAR samples are excluded from the regression. Radiogenic isotopes and Se isotopes for this sample set together with ambient depleted mantle values are from Douglass *et al.* (1999), Andres *et al.* (2002), and Yierpan *et al.* (2020).

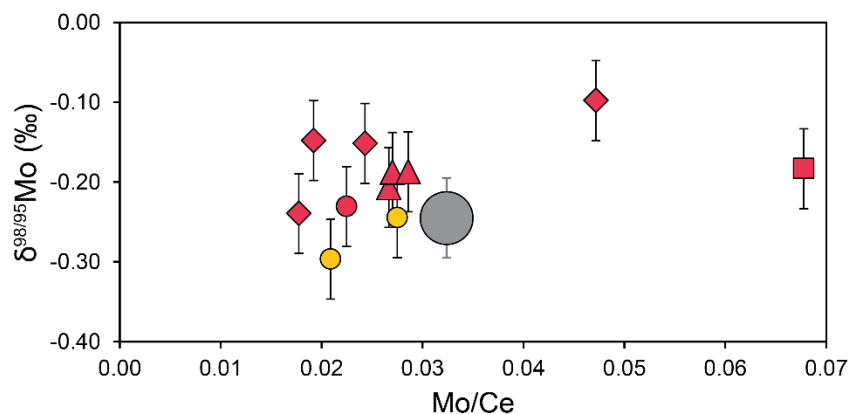


**Figure S-5** Covariation diagram of S-MAR samples with  $\delta^{98/95}\text{Mo}$  vs. Mo/Ce. Ce contents of samples and depleted mantle Mo/Ce are from Salters and Stracke (2004) and Kelley *et al.* (2013).

## Supplementary Information References

- Ahmad, Q., Wille, M., König, S., Rosca, C., Hensel, A., Pettke, T., Hermann, J. (2021) The Molybdenum isotope subduction recycling conundrum: A case study from the Tongan subduction zone, Western Alps and Alpine Corsica. *Chemical Geology* 576, 120231. <https://doi.org/10.1016/j.chemgeo.2021.120231>
- Andres, M., Blichert-Toft, J., Schilling, J.-G. (2002) Hafnium isotopes in basalts from the southern Mid-Atlantic Ridge from 40°S to 55°S: Discovery and Shona plume–ridge interactions and the role of recycled sediments. *Geochemistry, Geophysics, Geosystems* 3, 1–25. <https://doi.org/10.1029/2002GC000324>
- Bezard, R., Fischer-Gödde, M., Hamelin, C., Brennecke, G.A., Kleine, T. (2016) The effects of magmatic processes and crustal recycling on the molybdenum stable isotopic composition of Mid-Ocean Ridge Basalts. *Earth and Planetary Science Letters* 453, 171–181. <https://doi.org/10.1016/j.epsl.2016.07.056>
- Burkhardt, C., Hin, R.C., Kleine, T., Bourdon, B. (2014) Evidence for Mo isotope fractionation in the solar nebula and during planetary differentiation. *Earth and Planetary Science Letters* 391, 201–211. <https://doi.org/10.1016/j.epsl.2014.01.037>
- Chen, S., Hin, R.C., John, T., Brooker, R., Bryan, B., Niu, Y., Elliott, T. (2019) Molybdenum systematics of subducted crust record reactive fluid flow from underlying slab serpentine dehydration. *Nature Communications* 10, 4773. <https://doi.org/10.1038/s41467-019-12696-3>
- Chen, S., Sun, P., Niu, Y., Guo, P., Elliott, T., Hin, R.C. (2022) Molybdenum isotope systematics of lavas from the East Pacific Rise: Constraints on the source of enriched mid-ocean ridge basalt. *Earth and Planetary Science Letters* 578, 117283. <https://doi.org/10.1016/j.epsl.2021.117283>
- Douglass, J., Schilling, J.-G., Kingsley, R.H., Small, C. (1995) Influence of the discovery and Shona mantle plumes on the southern Mid-Atlantic Ridge: Rare earth evidence. *Geophysical Research Letters* 22, 2893–2896. <https://doi.org/10.1029/95GL02665>
- Douglass, J., Schilling, J.-G., Fontignie, D. (1999) Plume-ridge interactions of the Discovery and Shona mantle plumes with the southern Mid-Atlantic Ridge (40°–55°S). *Journal of Geophysical Research: Solid Earth* 104, 2941–2962. <https://doi.org/10.1029/98JB02642>
- Frey, H., Vils, F., Willbold, M., Taylor, R.N., Elliott, T. (2015) Molybdenum mobility and isotopic fractionation during subduction at the Mariana arc. *Earth and Planetary Science Letters* 432, 176–186. <https://doi.org/10.1016/j.epsl.2015.10.006>
- Gale, A., Dalton, C.A., Langmuir, C.H., Su, Y., Schilling, J.-G. (2013) The mean composition of ocean ridge basalts. *Geochemistry, Geophysics, Geosystems* 14, 489–518. <https://doi.org/10.1029/2012GC004334>
- Goldberg, T., Gordon, G., Izon, G., Archer, C., Pearce, C.R., McManus, J., Anbar, A.D., Rehkämper, M. (2013) Resolution of inter-laboratory discrepancies in Mo isotope data: an intercalibration. *Journal of Analytical Atomic Spectrometry* 28, 724–735. <https://doi.org/10.1039/c3ja30375f>
- Greaney, A.T., Rudnick R.L., Romaniello, S.J., Anbar, A.D. (2018) Completing the Molybdenum Isotope Mass Balance in Subduction Zones. *Goldschmidt Abstracts* 872. <https://goldschmidtabstracts.info/abstracts/abstractView?id=2018001568>
- Greaney, A.T., Rudnick, R.L., Romaniello, S.J., Johnson, A.C., Gaschnig, R.M., Anbar, A.D. (2020) Molybdenum isotope fractionation in glacial diamictites tracks the onset of oxidative weathering of the continental crust. *Earth and Planetary Science Letters* 534, 116083. <https://doi.org/10.1016/j.epsl.2020.116083>
- Greber, N.D., Siebert, C., Nägler, T.F., Pettke, T. (2012)  $\delta^{98/95}\text{Mo}$  values and Molybdenum Concentration Data for NIST SRM 610, 612 and 3134: Towards a Common Protocol for Reporting Mo Data. *Geostandards and Geoanalytical Research* 36, 291–300. <https://doi.org/10.1111/j.1751-908X.2012.00160.x>
- Greber, N.D., Pettke, T., Nägler, T.F. (2014) Magmatic–hydrothermal molybdenum isotope fractionation and its relevance to the igneous crustal signature. *Lithos* 190–191, 104–110. <https://doi.org/10.1016/j.lithos.2013.11.006>
- Hamelin, C., Dosso, L., Hanan, B.B., Moreira, M., Kositsky, A.P., Thomas, M.Y. (2011) Geochemical portrayal of the Pacific Ridge: New isotopic data and statistical techniques. *Earth and Planetary Science Letters* 302, 154–162. <https://doi.org/10.1016/j.epsl.2010.12.007>
- Kelley, K.A., Kingsley, R., Schilling, J.-G. (2013) Composition of plume-influenced mid-ocean ridge lavas and glasses from the Mid-Atlantic Ridge, East Pacific Rise, Galápagos Spreading Center, and Gulf of Aden. *Geochemistry, Geophysics, Geosystems* 14, 223–242. <https://doi.org/10.1002/ggge.20049>



- König, S., Rosca, C., Kurzawa, T., Varas-Reus, M.I., Dragovic, B., Schoenberg, R., John, T. (2021) Selenium isotope evidence for pulsed flow of oxidative slab fluids. *Geochemical Perspectives Letters* 17, 27–32. <https://doi.org/10.7185/geochemlet.2110>
- Labidi, J., Cartigny, P., Moreira, M. (2013) Non-chondritic sulphur isotope composition of the terrestrial mantle. *Nature* 501, 208–211. <https://doi.org/10.1038/nature12490>
- le Roux, P., le Roex, A., Schilling, J.-G. (2002a) Crystallization processes beneath the southern Mid-Atlantic Ridge (40–55°S), evidence for high-pressure initiation of crystallization. *Contributions to Mineralogy and Petrology* 142, 582–602. <https://doi.org/10.1007/s00410-001-0312-y>
- le Roux, P., le Roex, A., Schilling, J.G. (2002b) MORB melting processes beneath the southern Mid-Atlantic Ridge (40–55°S): a role for mantle plume-derived pyroxenite. *Contributions to Mineralogy and Petrology* 144, 206–229. <https://doi.org/10.1007/s00410-002-0376-3>
- le Roux, P.J., le Roex, A.P., Schilling, J.G., Shimizu, N., Perkins, W.W., Pearce, N.J.G. (2002c) Mantle heterogeneity beneath the southern Mid-Atlantic Ridge: trace element evidence for contamination of ambient asthenospheric mantle. *Earth and Planetary Science Letters* 203, 479–498. [https://doi.org/10.1016/S0012-821X\(02\)00832-4](https://doi.org/10.1016/S0012-821X(02)00832-4)
- Liang, Y.-H., Halliday, A.N., Siebert, C., Fitton, J.G., Burton, K.W., Wang, K.-L., Harvey, J. (2017) Molybdenum isotope fractionation in the mantle. *Geochimica et Cosmochimica Acta* 199, 91–111. <https://doi.org/10.1016/j.gca.2016.11.023>
- Lyons, T.W., Reinhard, C.T., Planavsky, N.J. (2014) The rise of oxygen in Earth's early ocean and atmosphere. *Nature* 506, 307–315. <https://doi.org/10.1038/nature13068>
- McCoy-West, A.J., Chowdhury, P., Burton, K.W., Sossi, P., Nowell, G.M., Fitton, J.G., Kerr, A.C., Cawood, P.A., Williams, H.M. (2019) Extensive crustal extraction in Earth's early history inferred from molybdenum isotopes. *Nature Geoscience* 12, 946–951. <https://doi.org/10.1038/s41561-019-0451-2>
- Moreira, M., Staudacher, T., Sarda, P., Schilling, J.-G., Allègre, C.J. (1995) A primitive plume neon component in MORB: The Shona ridge-anomaly, South Atlantic (51–52°S). *Earth and Planetary Science Letters* 133, 367–377. [https://doi.org/10.1016/0012-821X\(95\)00080-V](https://doi.org/10.1016/0012-821X(95)00080-V)
- Nebel-Jacobsen, Y., Wille, M., Ivanic, T., Nebel, O. (2021) Molybdenum isotope systematics in cumulate rock of the 2.8 Windimurra layered intrusion: A test for igneous differentiation and the composition of the Archean mantle. *Precambrian Research* 355, 106087. <https://doi.org/10.1016/j.precamres.2020.106087>
- Plank, T. (2014) 4.17 - The Chemical Composition of Subducting Sediments. In: Holland, H.D., Turekian, K.K. (Eds.) *Treatise on Geochemistry*. Second Edition, Elsevier, Oxford, 607–629. <https://doi.org/10.1016/B978-0-08-095975-7.00319-3>
- Rehkämper, M., Hofmann, A.W. (1997) Recycled ocean crust and sediment in Indian Ocean MORB. *Earth and Planetary Science Letters* 147, 93–106. [https://doi.org/10.1016/S0012-821X\(97\)00009-5](https://doi.org/10.1016/S0012-821X(97)00009-5)
- Rudnick, R.L., Gao, S. (2014) 4.1 - Composition of the Continental Crust. In: Holland, H.D., Turekian, K.K. (Eds.) *Treatise on Geochemistry*. Second Edition, Elsevier, Oxford, 1–51. <https://doi.org/10.1016/B978-0-08-095975-7.00301-6>
- Salters, V.J.M., Stracke, A. (2004) Composition of the depleted mantle. *Geochemistry, Geophysics, Geosystems* 5, Q05B07. <https://doi.org/10.1029/2003GC000597>
- Sarda, P., Moreira, M., Staudacher, T., Schilling, J.-G., Allègre, C.J. (2000) Rare gas systematics on the southernmost Mid-Atlantic Ridge: Constraints on the lower mantle and the Dupal source. *Journal of Geophysical Research: Solid Earth* 105, 5973–5996. <https://doi.org/10.1029/1999JB900282>
- Siebert, C., Nägler, T.F., Kramers, J.D. (2001) Determination of molybdenum isotope fractionation by double-spike multicollector inductively coupled plasma mass spectrometry. *Geochemistry, Geophysics, Geosystems* 2, 2000GC000124. <https://doi.org/10.1029/2000GC000124>
- Stracke, A. (2012) Earth's heterogeneous mantle: A product of convection-driven interaction between crust and mantle. *Chemical Geology* 330–331, 274–299. <https://doi.org/10.1016/j.chemgeo.2012.08.007>
- Voegelin, A.R., Pettke, T., Greber, N.D., von Niederhäusern, B., Nägler, T.F. (2014) Magma differentiation fractionates Mo isotope ratios: Evidence from the Kos Plateau Tuff (Aegean Arc). *Lithos* 190–191, 440–448. <https://doi.org/10.1016/j.lithos.2013.12.016>
- Vollmer, R. (1976) Rb-Sr and U-Th-Pb systematics of alkaline rocks: the alkaline rocks from Italy. *Geochimica et Cosmochimica Acta* 40, 283–295. [https://doi.org/10.1016/0016-7037\(76\)90205-2](https://doi.org/10.1016/0016-7037(76)90205-2)
- Wang, Z., Becker, H. (2018) Molybdenum partitioning behavior and content in the depleted mantle: Insights from Balmuccia and Baldissero mantle tectonites (Ivrea Zone, Italian Alps). *Chemical Geology* 499, 138–150. <https://doi.org/10.1016/j.chemgeo.2018.09.023>



- Willbold, M., Elliott, T. (2017) Molybdenum isotope variations in magmatic rocks. *Chemical Geology* 449, 253–268. <https://doi.org/10.1016/j.chemgeo.2016.12.011>
- Willbold, M., Hibbert, K., Lai, Y.-J., Freymuth, H., Hin, R.C., Coath, C., Vils, F., Elliott, T. (2016) High-Precision Mass-Dependent Molybdenum Isotope Variations in Magmatic Rocks Determined by Double-Spike MC-ICP-MS. *Geostandards and Geoanalytical Research* 40, 389–403. <https://doi.org/10.1111/j.1751-908X.2015.00388.x>
- Wille, M., Nebel, O., Van Kranendonk, M.J., Schoenberg, R., Kleinhanns, I.C., Ellwood, M.J. (2013) Mo–Cr isotope evidence for a reducing Archean atmosphere in 3.46–2.76 Ga black shales from the Pilbara, Western Australia. *Chemical Geology* 340, 68–76. <https://doi.org/10.1016/j.chemgeo.2012.12.018>
- Wille, M., Nebel, O., Pettke, T., Vroon, P.Z., König, S., Schoenberg, R. (2018) Molybdenum isotope variations in calc-alkaline lavas from the Banda arc, Indonesia: Assessing the effect of crystal fractionation in creating isotopically heavy continental crust. *Chemical Geology* 485, 1–13. <https://doi.org/10.1016/j.chemgeo.2018.02.037>
- Yang, J., Siebert, C., Barling, J., Savage, P., Liang, Y.-H., Halliday, A.N. (2015) Absence of molybdenum isotope fractionation during magmatic differentiation at Hekla volcano, Iceland. *Geochimica et Cosmochimica Acta* 162, 126–136. <https://doi.org/10.1016/j.gca.2015.04.011>
- Yang, J., Barling, J., Siebert, C., Fietzke, J., Stephens, E., Halliday, A.N. (2017) The molybdenum isotopic compositions of I-, S- and A-type granitic suites. *Geochimica et Cosmochimica Acta* 205, 168–186. <https://doi.org/10.1016/j.gca.2017.01.027>
- Ye, Y., Zhang, S., Wang, H., Wang, X., Tan, C., Li, M., Wu, C., Canfield, D.E. (2021) Black shale Mo isotope record reveals dynamic ocean redox during the Mesoproterozoic Era. *Geochemical Perspectives Letters* 18, 16–21. <https://doi.org/10.7185/geochemlet.2118>
- Yierpan A., König S., Labidi J., Schoenberg R. (2019) Selenium isotope and S-Se-Te elemental systematics along the Pacific-Antarctic ridge: Role of mantle processes. *Geochimica et Cosmochimica Acta* 249, 199–224. <https://doi.org/10.1016/j.gca.2019.01.028>
- Yierpan, A., König, S., Labidi, J., Schoenberg, R. (2020) Recycled selenium in hot spot-influenced lavas records ocean-atmosphere oxygenation. *Science Advances* 6, abb6179. <https://doi.org/10.1126/sciadv.abb6179>
- Yierpan A., Redlinger J., König S., (2021) Selenium and tellurium in Reykjanes Ridge and Icelandic basalts: Evidence for degassing-induced Se isotope fractionation. *Geochimica et Cosmochimica Acta* 313, 155–172. <https://doi.org/10.1016/j.gca.2021.07.029>
- Zhao, P.-P., Li, J., Zhang, L., Wang, Z.-B., Kong, D.-X., Ma, J.-L., Wei, G.-J., Xu, J.-F. (2016) Molybdenum Mass Fractions and Isotopic Compositions of International Geological Reference Materials. *Geostandards and Geoanalytical Research* 40, 217–226. <https://doi.org/10.1111/j.1751-908X.2015.00373.x>

